Title

EVIDENCE FOR DIFFUSIVE RELAXATION ALONG THE MASS ASYMMETRY COORDINATE IN THE REACTION 197Au + 620 MeV 86Kr

Author

Russo, P.

Publication Date

1976-11-01

Submitted to Nuclear Physics

LBL-5810
Preprint

EVIDENCE FOR DIFFUSIVE RELAXATION ALONG THE MASS ASYMMETRY COORDINATE IN THE REACTION ^{197}Au + 620 MeV ^{86}Kr

P. Russo, R. P. Schmitt, G. J. Wozniak, R. C. Jared,
P. Glässel, B. Cauvin, J. S. Sventek, and L. G. Moretto

November 1976

Prepared for the U. S. Energy Research and
Development Administration under Contract W-7405-ENG-48

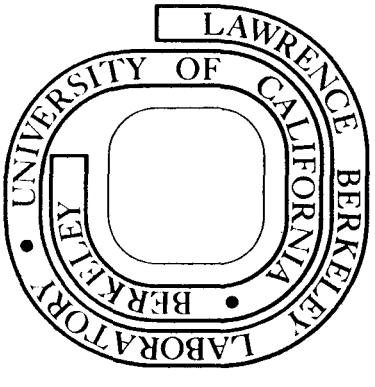

DISCLAIMER

LBL-5810

EVIDENCE FOR DIFFUSIVE RELAXATION ALONG THE MASS ASYMMETRY COORDINATE IN THE REACTION ^{197}Au + 620 MeV ^{86}Kr*

P. Russo[+], R. P. Schmitt, G. J. Wozniak, R. C. Jared, P. Glässel[++], B. Cauvin[‡], J. S. Sventek and L. G. Moretto[**]

Department of Chemistry
and
Lawrence Berkeley Laboratory
University of California
Berkeley, California 94720

ABSTRACT

Nuclei have been identified by atomic number up to Z = 50 using ΔE-E telescopes. Kinetic energy spectra, charge and angular distributions have been measured from θ_{lab} = 10-80°. At angles removed from the grazing, a single peak with a mean energy somewhat below the calculated Coulomb energy is observed for all elements. Near the grazing angle, a much broader peak appears, which extends from near elastic energies down to the Coulomb barrier. The charge distributions were peaked near the projectile Z and demonstrate a strong shape dependence on the angle of observation. The angular distributions for elements near the projectile are strongly side-peaked; however, as Z is increased or decreased from Z = 36 they gradually become forward peaked. The dependence of the charge and angular distributions on energy dissipation is discussed as well as the patterns observed in the two-dimensional Wilczynski plots. Diffusion model calculations reproduce the experimental data both qualitatively and quantitatively. This successful application of the diffusion model, which was originally developed to explain N, Ne and Ar induced reactions, to the present

system is strong evidence that no essential differences exist between the "quasi-fission" process observed in Kr bombardments of heavy targets and the deep-inelastic phenomena seen with lighter ions.

E NUCLEAR REACTIONS $^{197}Au(^{86}Kr,Z)$, for $14 \leq Z \leq 55$; E_{lab} = 620 MeV; measured $\sigma(E,Z,\theta)$; deduced: mass diffusion constant, lifetimes of intermediate complex.

* This work was done with support from the U.S. Energy Research and Development Administration.

+ Present address: University of Rochester, Rochester, New York 14627.

++ Nato Fellow .

‡ Present address: DphN/MF-CEN, Saclay, France.

** Sloan Fellow 1974-1976.

1. Introduction

Rather remarkably, nuclear reactions induced by simple projectiles such as p, d and α particles can be categorized as either direct or compound nuclear reactions. These processes are distinguished from each other by the number of degrees of freedom involved, the time scale and the extent to which the entrance and exit channels are coupled. Direct interactions typically involve only a few specific degrees of freedom, occur on a short time scale (10^{-21} to 10^{-22} sec) and exhibit strong coupling between entrance and exit channels. On the other hand, compound nuclear reactions proceed through the formation of a long lived ($\sim 10^{-18}$ sec) intermediate system which is equilibrated in all nuclear degrees of freedom (i.e. the compound nucleus) and, aside from the constraints of conservation laws, show complete decoupling of the entrance and exit channels.

When heavier projectiles are employed, this dichotomy breaks down, and, in addition to compound nuclear and direct reactions, one observes a variety of phenomena which reflect varying degrees of relaxation towards equilibrium.[1-3] Broad charge distributions have been observed for the deep-inelastic or energetically relaxed products from the bombardments of a variety of targets at energies well above the Coulomb barrier. The nearly thermalized energy spectra of these products were reminiscent of the fission process and the shapes of the charge distributions Y(Z) were in rough qualitative agreement with the statistical prediction:

$$Y(Z) \propto e^{-V_Z/T} , \qquad (3)$$

where T is the temperature and V_Z is the liquid drop potential energy for touching spherical fragments.[4] However, detailed studies[4-7] of

reactions leading to similar compound nuclei (Ag + N, Ag + Ne and Ag + Ar) reveal that the pattern of the charge distributions depends strongly on the entrance channel, indicating that such deep-inelastic products are the result of a non-equilibrium process that does not proceed through the formation of a compound nucleus. This was also indicated by the angular distributions which are forward-peaked in excess of $1/\sin\theta$. These observations have been interpreted as evidence for an intermediate complex consisting of two touching fragments which evolves along the mass/charge asymmetry mode via a diffusion process.[8,9] Moretto and Sventek have developed a model employing the Master Equation and have obtained quantitative agreement[10] with the experimental charge and angular distributions of products formed in the reaction ^{107,109}Ag + 288 MeV ^{40}Ar.

Early experiments with Kr projectiles at center of mass energies of about 1.5 times the Coulomb barrier revealed features so different from those seen with lighter projectiles that a new mechanism, "quasi-fission", was postulated.[11,12] Although the "quasi-fission" fragments had Coulomb-like energies, their relatively narrow mass distributions were peaked near the projectile mass, and the gross product (all masses) angular distributions were side-peaked. In order to clarify the experimental situation for such heavy systems, we have applied the technique of elemental (Z) identification to the system of ^{197}Au + 620 MeV ^{86}Kr. A brief report of this work has appeared in ref.[13]

2. Experimental Technique

Beams of 620 MeV ^{86}Kr from the Berkeley Super-HILAC were utilized to bombard 0.45 mg/cm^2 natural, self-supporting ^{197}Au foils. Beam intensities of 5 - 50 nA (q = +32) were readily obtained with dead time and pileup considerations limiting the intensity at forward angles. A forward-angle out-of-plane counter monitored the beam energy and was also utilized to detect the presence of parasitic beams, which were eliminated with proper tuning of the accelerator. To monitor shifts in the gain or baseline, pulser signals were fed into the system both during and between beam bursts.

Reaction products were detected with four telescopes mounted in pairs on opposite sides of the scattering chamber, each consisting of a gas ionization ΔE counter and a 400 μ solid state E counter.[14] At forward angles the gas counter entrance windows were 0.28 mg/cm^2 polycarbonate (Kimfoil) foils and at more backward angles 0.04 mg/cm^2 Formvar foils. The gas counters operated with pure methane (CH_4) gas at pressures between 50 and 300 Torr and at flow rates of $\sim$ 0.1 ℓ/sec. These pressures and flow rates were independently regulated for the more forward and more backward pairs of counters to better than 0.5% with Cartesian manostats. To identify events with Z = 40 from those with Z = 41, the ΔE thickness must be fixed to better than $\simeq$ 2%, thus it was important that the CH_4 density was well regulated.

The telescope acceptance angles of 1° to 2.5° were defined by circular collimators with diameters of 0.1 to 0.3 cm. The absolute solid angles of the telescopes were determined with an ^{241}Am α-source

of known activity. Elastic scattering measurements at both positive and negative angles were made to determine the scattering chamber asymmetry.

Two parameter (ΔE, E) event-by-event data were taken with a multiplexer analog-to-digital converter system and written on magnetic tape with a PDP-15 computer. On-line monitoring was accomplished with a two dimensional display of E and ΔE on a storage scope. In addition, the solid state E counter was inspected for radiation damage by observing the position and width of the elastic line ($\sim$10 MeV FWHM) in four separate one-dimensional displays. The Z-resolution of each telescope was monitored off-line by printing expanded E - ΔE arrays with a PDP-9 computer.

Event-by-event data were sorted off-line into two-dimensional ΔE versus E maps (960 $\times$ 100 channels). A computerized technique[15] was used for the automatic location and subsequent fitting of ridges corresponding to individual elements in the two-dimensional map. The prominent projectile ridge determined the absolute Z calibration. In order to systematically locate these ridges, a triangular function was convoluted with the data in a narrow cut in E along the ΔE coordinate. This folding integral oscillates through maxima and minima as a function of ΔE due to the periodic superposition of the triangle with the ridges and valleys, respectively. The grid of ridge points generated by the maxima defined the Z-ridges, and the limits for individual Z's were chosen midway between the ridge lines.

An energy calibration of the E amplifier systems was obtained from a precision mercury pulser that was calibrated at low energies with a ^{241}Am α - source and at high energies with elastically scattered Kr ions whose pulse heights were suitably corrected for energy losses in the target, in the gas counter window and the dead layer of the solid state counter. These calibration data were collected with the gas counter evacuated. The shift in the energy of the E signal for runs with and without gas in the telescope along with the mercury pulser were used to calibrate the ΔE amplifier system.

Laboratory energies of the detected fragments were corrected for losses in the target and gas windows using polynomial fits to Northcliffe and Schilling range-energy data.[16] The pulse-height defect in the solid state counter was determined in sub-barrier bombardments of heavy targets with argon projectiles through a coincidence measurement of the elastic argon and the recoil target nuclei. The Z-dependent pulse-height defect calibration was obtained as described by Kaufman, et al.[17] Uncertainties in the total laboratory fragment energy are of the order of 3% due to uncertainties in the beam energy and in the above corrections.

3. Results and Discussion

In this section center-of-mass kinetic energy spectra, charge and angular distributions are presented for over 30 identified elements. The number of elements that were identified is dependent on the fragment energy, more being resolved at forward angles where the energy is highest. These experimental results are compared to those from other projectile-target combinations and to the diffusion model calculations of Moretto and Sventek.[10]

In Table I, the values of a number of parameters which characterize the system ^{197}Au + 620 MeV ^{86}Kr are listed. One should note that the ratio of the center of mass energy to the Coulomb barrier of 1.5 for this reaction is somewhat small compared to a typical $E/B \gtrsim 2$ for most light ion reactions we have previously studied,[4-7] and that the maximum angular momentum is very large $\sim 300\ \hbar$. Furthermore, the grazing angle is 58° ($\theta_{c.m.}$) and the rotational period of the intermediate complex is about 10^{-20} seconds.

3.1 KINETIC ENERGY SPECTRA

To generate kinetic energy spectra for each identified element, a two-dimensional gate was set around each element ridge and laboratory energy spectra were projected out. To transform these spectra to the center of mass system, one must know the fragment mass. Direct A and Z measurements for fragments produced in the reaction Ni + Ar support a charge equilibrium model.[18] In this model, the mean pre-evaporative Z is the one which minimizes the liquid drop potential energy for fixed mass asymmetry. This model has been confirmed with coincidence measurements for a slightly heavier system ^{107,109}Ag + 288 MeV ^{40}Ar.[19]

The fragment mass calculated from the charge equilibrium model was utilized to make the lab to center-of-mass transformation, neglecting the effect of light-particle evaporation (n,p and α) on the fragment masses and energies.

To first order, the energy before evaporation E^* is given by:

$$E^* = E/(1 - \nu/m) \ , \qquad (1)$$

where E, m, and ν are the energy after evaporation, the mass before evaporation and the evaporated mass, respectively. To accurately correct for the neglect of particle evaporation, one must know the fragment mass before evaporation and the number of evaporated nucleons. However, if the quantity ν/m is small, the error in the mean center of mass energies due to this effect is given by the expression:

$$\Delta = E^* - E = \left[E_{lab} - \sqrt{\frac{m m_p E_p E_{lab}}{M_T^2}} \cos\theta \right] \cdot \frac{\nu}{m} \ , \qquad (2)$$

where E_{lab} and θ are the observed laboratory energy and angle of the fragment, m_p and E_p are the projectile mass and energy and M_T is the total mass of the system. Even pessimistic assumptions of the number of evaporated particles result in corrections of at most 7%.

Center-of-mass kinetic energy spectra from the reaction 620 MeV $^{86}Kr + ^{197}Au$ for a number of elements are shown in Fig. 1 for selective angles: before (18.8°), near (35.4°) and behind (60.4°) the grazing angle ($\theta_{lab} = 41°$). Although energy spectra were obtained for each of the $\sim$ 30 elements identified at each angle, the spectral shapes change slowly with Z so only a few representative cases are depicted here. The atomic number of an element's energy spectra is noted only once on the left of

the 18.8° data. To illustrate how an energy spectrum would look if the individual elements were not identified, a "total" spectrum is shown for each angle at the bottom of the columns in Fig. 1. In these "total" spectra, the center-of-mass energies were obtained by assuming that all events had the mass of the projectile.

Glancing down the column of Fig. 1, one is struck by the preponderance of cross section in the broad peak occurring near the Coulomb energies for two touching spheres (arrows). An inspection of the location and width of this broad peak for both the forward and backward angle data shows that, to first order, they are constant for all of the detected elements, indicating a nearly complete relaxation of the kinetic energy.

For elements close to the projectile at 35.4°, the uniformity of the energy spectra is violated. For these elements the spectra show a much broader structure extending to energies substantially above the calculated Coulomb barrier, indicating large contributions from quasi-elastic or incompletely damped events. The higher energy events are clearly more numerous than the relaxed events for Z = 32 and 36 while the two contributions are approximately equal for Z = 40. The continuous evolution observed in the degree of damping from the deep inelastic to the quasi-elastic makes it difficult to reliably determine their individual magnitudes.

3.2 MEAN KINETIC ENERGY

Mean energies and full-widths-at-half-maximum were extracted from the broad peaks observed in Fig. 1 after the subtraction of background due to elastic and slit scattered projectiles, recoiling transfer products

and low energy elastic scattering of target nuclei (e.g. see intense low-energy tail in 60.4° data of Fig. 1). In Fig. 2 the extracted mean energies (open circles) and widths (open squares) for each identified element averaged over angles both fore and aft of the grazing angle are shown. The "error bars" represent a one standard deviation spread in the data. Their relatively small size indicates the complete damping of the initial system's kinetic energy for all elements at most angles.

To illustrate the case of partial damping, the 40.4° data (shaded symbols) are also shown (no attempt was made to separate the strongly overlapping quasi-elastic and deep inelastic components at this angle). A sharp peak is produced near Z = 36 in both the mean energies and widths by the large quasi-elastic component; whereas, the data for elements far above or below the projectile fall within one standard deviation of the average values for the relaxed energies (open symbols). Thus Fig. 2 illustrates the occurrence of partial damping for elements near the projectile and angles near the critical angle, and the complete relaxation of the kinetic energies over the entire angular range (10 - 80°) for elements below Z = 29 and above Z = 41. Since incomplete energy damping is only observed for relatively small mass transfers, energy damping appears to occur more rapidly than mass transfer.

An additional interesting feature illustrated in Fig. 2 is the 20% difference between the experimental mean values (open circles) and the Coulomb energies calculated from the repulsion of two touching spheres (solid curve). In general, the relaxed energies follow the

trend of the curve but lie somewhat below it. The experimental center-of-mass energies have not been corrected for particle evaporation (see earlier discussion), and the solid curve does not include the rotational energy of the complex. Because these two effects are similar in magnitude, their combined effect should not appreciably change the separation between the data points and the calculated curve. Thus the 20% shift below the calculated Coulomb energies for spheres is probably the result of fragment deformation. Data[7,20] from 288 MeV ^{40}Ar and 979 MeV ^{136}Xe on ^{197}Au add additional support to the fragment deformation hypothesis. For elements near the projectile, the shift below Coulomb energies is 12% for the Ar + Au system[7] and 30% for the Xe + Au data.[20] Thus the increasing deformability of the heavier systems manifests itself in a larger decrease of the fragment center-of-mass kinetic energy below the calculated Coulomb energies for two touching spheres.

3.3 EXPERIMENTAL CHARGE DISTRIBUTIONS AND DIFFUSION CALCULATIONS

The measured laboratory charge distributions for the reaction ^{197}Au + 620 MeV ^{86}Kr are given in Fig. 3 for a wide range of laboratory angles. In general they tend to be narrow in comparison with those obtained in Ar bombardments at high energies.[6,7] Moreover, there is a strong shape dependence of these Z-distributions on the angle of observation. At forward angles, they are rather broad and are centered near the projectile Z. As the detection angle increases, a narrow peak develops around the projectile atomic number. For the most backward angles, the Z-distributions are broadest and are shifted toward heavier elements, although the experimental Z cutoff makes it difficult to accurately locate their maxima.

The displacements in the Z-distribution centroids and the large width variations can be attributed to differences in the system interaction time. For diffusion along a linear potential, the solution of the Fokker-Planck equation[21,22] yields:

$$\langle Z \rangle = Z_0 + \mu_1 t, \tag{4}$$

and

$$\sigma_z^2 = \mu_2 t, \tag{5}$$

where Z_0, $\langle Z \rangle$, σ_z^2 are the initial Z, the average Z, the variance of the charge distributions and the time. The quantities μ_1 and μ_2 are the drift and spreading coefficients, respectively. While one does not expect that a linear potential represents the physical situation, for a variety of potential shapes one would expect that eqs. 4 and 5 are qualitatively correct in their predictions: short times imply little drift from the entrance channel asymmetry and small charge widths.

Realistic potential energies, calculated using the liquid drop model and the assumption that the complex consists of two interpenetrating spheres, are shown in Fig. 4 for several ℓ-waves (0, 80, 160 and 240 $\hbar$). Each curve has been calculated relative to the injection point potential energy (Z of the projectile). It should be noted that the injection point for this system is to the right of the Businaro-Gallone mountain and that a negative slope of the potential at the injection point favors the transfer of matter from the target to the projectile. An example of the population probabilities calculated with the diffusion model for $\ell = 0$ (see Fig. 4) are presented in Fig. 5a as contours of

constant population in the plane defined by the charge asymmetry and the time. The drift of the distributions from the injection point towards symmetry (low potential energy) with increasing time is well illustrated. Perhaps more impressive is the rapid spread in width of the distributions with time which is accentuated by the overlap of the target and projectile distributions.

Returning to Fig. 4, one notes that the slope of the potential at the injection point increases dramatically for increasing ℓ. Thus for the low ℓ-waves, the driving force toward symmetry is small. Because of the high temperature the system can spread over a broad range of charge asymmetries. When the angular momentum is increased, the potential well at symmetry becomes deeper. Thus the system is more quickly driven towards symmetry. The effects of the angular momentum-dependent driving potential on the population probabilities (calculated with the potentials shown in Fig. 4) are beautifully illustrated in Figs. 5a,b,c, and d. The narrowing of the population distributions for high ℓ values is particularly apparent in Fig. 5d and is due to a drastic reduction in the nuclear temperature because of energy tied up in rotation.

Since the usefulness of the Fokker-Planck approximation to the Master equation has been dealt with elsewhere,[22] it will not be discussed in detail here. However, it should be noted that the linear relation between σ_z^2 and $\langle Z \rangle - Z_0$ predicted by Eqs. 4 and 5 is appproximately borne out by the calculations (see Fig. 5). This linear dependence is better illustrated by the calculations shown in Fig. 6. While for any individual ℓ, σ_z^2 increases nearly linearly, the slope varies drastically with ℓ.

It is important to note that, irrespective of details of the models (Fokker-Planck or Master equation) or the ℓ-wave dependence, the width and the displacement of the charge distributions increase with time. This leads to the association of the narrow Z-distributions observed at near grazing incidence with short interaction times. Thus one can label these distributions as "young". Similarly, the intermediate width distributions at forward angles and the broad distributions at backward angles may be described as "middle-aged" and "old", respectively.

The variation in the shape and centroid of the Z-distribution with angle can be understood qualitatively if one assumes that the intermediate-complex lifetime increases with decreasing impact parameter (or angular momentum). For large values of the impact parameter b, the small radial velocity results in little internuclear penetration. Under these conditions the complex is short-lived or "young". Because of these short lifetimes, little mass is transferred and only small angular displacements occur yielding narrow ("young") distributions near the grazing angle. For intermediate values of b, the lifetime is long enough ("middle aged") for considerable mass transfer and relatively large angular displacements to occur. In fact, the composite system may rotate to angles forward of the grazing before decaying.

Small impact parameters involve the largest radial velocities, maximum interpenetration and therefore the longest lifetimes ("old"). While these long lifetimes allow the diffusion to reach a more advanced state, the low angular velocities permit only a small rotation of the complex before decay so that emission occurs largely behind the grazing angle.

Unlike the "young" and "middle-aged" distributions, the "old" distributions (backward angles) show a substantial shift towards symmetry.

Since the qualitative features of the angular dependence of the charge distributions can be explained in terms of a diffusion process with an ℓ-dependent lifetime, we were encouraged to perform detailed calculations in an attempt to quantitatively reproduce the data. Diffusion model calculations for the ^{197}Au + 620 MeV ^{86}Kr system have been performed previously by Sventek and Moretto[23,24] assuming that the complex consisted of two touching spheres and that

$$\tau(\ell) = \tau(0)(1 - \ell/\ell_{max}) \ , \qquad (6)$$

where $\tau(\ell)$ is the lifetime of the complex for angular momentum (ℓ). The assumed linear relationship between τ and ℓ is reasonable in light of dynamical treatments.[25] The various parameters in the model (see ref. 24) were grossly adjusted to reproduce the experimental charge and angular distributions. In order to obtain reasonable agreement, a diffusion constant K whose value was one-half of that obtained from fitting the angular distributions for the reaction ^{107,109}Ag + 288 MeV ^{40}Ar was used. These cross section calculations were in reasonable agreement with experimental data for atomic numbers with $Z \gtrsim 32$, and the variation of the Z-distributions with angle was qualitatively reproduced. However, the theory underestimated the yield of light elements by roughly an order of magnitude.

Since the diffusion constant K should be system independent apart from a geometrical form factor, reducing it by a factor of 2 represents a serious difficulty for the theory. The poor agreement for the lower

atomic numbers was thought to be the result of a potential energy that was too steep at the injection point rather than a failure of the theory. Too steep a slope drives the system too quickly toward symmetry at the expense of the yield for small atomic numbers. Reduction of the diffusion constant by a factor of two slows this drift toward symmetry, but also reduces the spreading, thus yielding poor agreement for elements considerably lighter than the projectile.

Since the potential energy depends on the assumed shape of the complex, it is reasonable to investigate the effect of different shapes on the diffusion process. For simplicity the individual fragments were held spherical, and only the distance between their geometrical centers was allowed to vary; more explicitly

$$d = 1.225\ (A_1^{1/3} + A_2^{1/3}) + \delta \quad , \tag{7}$$

where d is the separation of the centers, A_1 and A_2 are the mass numbers of the fragments and δ is the new parameter.

It was found that positive values of δ led to poorer agreement as they increased the slope towards symmetry because of the smaller rotational energy associated with the more extended shapes. On the other hand, negative values of δ flatten the slope causing less displacement and allow more spreading of the Z-distributions. Fits to the integrated charge distributions obtained with δ = -2.0 fm are shown in Fig. 7. Impressive agreement between theory and experiment is observed. Both the shape and magnitude of the data are reproduced to approximately 50% with the largest deviations occurring for elements near the projectile where there are large quasi-elastic contributions (neglected in the

calculations which assume an upper ℓ cutoff of 252 $\hbar$).

The assumption of a more compact shape may seem at first to be in conflict with the elongated shapes implied by the mean fragment kinetic energies which lie below the calculated Coulomb energies for spheres using a δ of +2.0. However, the observed mean energies reflect the shape at scission rather than the time averaged shape which is the relevant one during the diffusion process. Dynamical calculations[26] indicate that an interprenetration of 2 fm is quite reasonable. In addition, we should point out that Eq. 7 yields d = 10.53 fm for the distance between the two centers of the complex, which is to be compared with 11.19 fm obtained from summing the half density radii calculated according to the prescription of Myers[27]. The most important question remaining is whether the previously studied Ag +Ar case[10] can be fitted when the interpenetration of fragments is taken into account. Preliminary calculations indicate that this can be done in a consistent manner with appropriate scaling.

Calculated charge distributions are presented in Fig. 8 for a variety of center of mass angles. To aid comparison with theory, "experimental" points have been obtained by linear interpolation between points in the angular distributions. Both the widths and the centroids of the calculated Z-distributions are in reasonable agreement with experiment except for angles where there is a large quasi-elastic contribution. The inclusion of higher ℓ-waves in the model calculations should improve the fit in these regions. Furthermore, the angular dependence of the width and magnitude of the Z-distributions is well predicted (except for 80°), supporting the hypothesis

of an ℓ-dependent lifetime. Calculated angular distributions utilizing the same parameters will be presented in the next section.

A total experimental reaction cross section of 2.2b is obtained by summing over all Z's in Fig. 7. This number is in reasonable agreement with the value of 2.3b for the calculated total reaction cross section given in Table I and with the value (1.9b) calculated from a radius constant[28] ($r_o = 1.38$) found in the literature. The absolute error in our total reaction cross section may be as large as 25% due to uncertainties in background subtraction, solid angle, target thickness, etc., and difficulties in resolving elastic and inelastic events for Z = 36.

Before ending the discussion of the experimental charge distributions, some comments should be made regarding the possible contribution to elements near Z = 42 from the fission of the Au-like deep-inelastic fragments. Recent experimental studies[20] of the reaction ^{197}Au + 979 MeV ^{136}Xe revealed bimodal kinetic energy spectra for products with Z near 42. The charge distributions and energy dependence on angle for the two peaks indicated that one of the components was due to the fission of Au-like fragments produced in the deep-inelastic process. While there is no direct evidence for secondary fission in the kinetic energy spectra of fragments produced in the reaction ^{197}Au + 620 MeV ^{86}Kr, simple calculations indicate that for most angles the fission fragments would have insufficient energy to be identified in Z under the present experimental conditions. For angles near 50° in the lab, where they should be observable, the expected energies overlap those of the abundant deep-inelastic component.

The charge distributions also fail to give an unambiguous answer to the question of whether any secondary fission yield is present. At backward angles there is a substantial population of elements near Z = 42, but the potential energy associated with the mass/charge asymmetry coordinate (see Fig. 4) decreases as one moves towards symmetry, so this yield can be accounted for as enhanced diffusion towards symmetry. In conclusion, while it is reasonable to expect some secondary fission of the Au-like fragments from the current reaction, no clear evidence is observed in the current experimental data. Future coincidence measurements are needed to resolve the issue.

3.4 ANGULAR DISTRIBUTIONS

From the discussion of the charge distributions in the last section, it is clear that the diffusion model predictions are in nearly quantitative agreement with the data. While this observation lends considerable support to the contention that the so-called "quasi-fission" phenomenon shares a common mechanism with the deep-inelastic process, the angular distributions for individual elements produced in the $^{197}Au + 620$ MeV ^{86}Kr reaction leave little doubt that this is indeed the case (see Fig. 9). These distributions are side-peaked for elements close to krypton, but forward peaked (in excess of $1/\sin\theta$) for elements far above or below krypton. A close inspection of Fig. 9 shows that the transition from side to forward peaking is continuous. As the atomic number of the fragment is increased or decreased from that of the projectile, the peak in the angular distributions moves to smaller angles, producing first a shoulder for intermediate mass transfers, and eventually disappearing for the largest mass transfers leaving forward peaked distributions.

Side-peaked angular distributions suggest that the lifetime of the complex is substantially shorter than the rotational period so that the system seldom rotates past 0°, causing the fragments to be emitted on the side of impact. This seems to be the case for elements close to Kr. For somewhat longer lifetimes one expects angular displacements towards 0° with a corresponding increase in yield at small angles. When the lifetime is sufficiently long, rotation past 0° is possible and causes a forward peaking in the angular distributions as is observed for elements well above or below the projectile. Such qualitative considerations lead one to the conclusion that the effective lifetime for the $^{197}Au + 620$ MeV ^{86}Kr system increases with increasing mass (charge) transfer.

The above observations are readily explained in terms of a diffusive evolution along the mass asymmetry mode. For a diffusive mechanism the spread in mass increases with time (see Fig. 5); therefore, the time delay in populating a given element should increase as the difference $|Z - Z_{proj}|$ increases. Thus the increasing time delay associated with larger and larger mass transfer can be correlated with the observed continuous transition from side to forward peaking in the experimental data.

Angular distributions calculated with the diffusion model of Moretto and Sventek are presented in Fig. 10 along with the experimental data for every other element. These distributions are presented (from top to bottom of Fig. 10) in order of increasing mass transfer to the target (left column) and to the projectile (right column). For elements above the projectile, the position and magnitude of the side peak as well as the shape of the experimental data are quite well reproduced.

For elements below the projectile, the magnitude of the side peak is underestimated, but its position as well as the magnitude of the backward angle points is correctly predicted. The large underestimation of the magnitude of the side peak observed for elements close to the projectile is due to the strong quasi-elastic contribution in the data (see Fig. 1) and the neglect of partially damped processes in the calculations. It should be stressed that no normalization between calculations and experiment has been performed.

From these calculations, the following values of the diffusion constant, κ, and lifetime for $\ell = 0$, $\tau(0)$ were obtained:

$$\kappa = 0.5 \times 10^{21} \text{ charge units sec}^{-1} \text{ fm}^{-2}, \qquad \tau(0) = 4.0 \times 10^{-21} \text{ sec.}$$

$$\begin{cases} \mu_1 = 3.0 \times 10^{21} \text{ charge units} \cdot \text{sec}^{-1} \\ \mu_2 = 0.66 \times 10^{22} \text{ (charge units)}^2 \text{ sec}^{-1} \end{cases}$$

(The values of μ_1 and μ_2 for the injection asymmetry were calculated from κ, see ref.[22]) As discussed in the last section, this value of κ is the same as that obtained from the ^{40}Ar fits. For the current reaction the value of $\tau(0)$ is rather accurately determined by the position of the side peak and, in agreement with the above discussion, is considerably smaller than the expected rotational period ($\sim 9 \times 10^{-20}$ sec). The quantity $\tau(0)$ should not be directly compared with the ℓ-independent lifetime used to fit the ^{107,109}Ag + 288 MeV ^{40}Ar data of reference 10.

Recent experiments[29,30,31] have been performed with Ag, Tb and Ta targets and Kr projectiles. In the case of Ag + Kr at 7.2 MeV/A, broad charge distributions peaked at symmetry and forward-peaked angular distributions were observed,[29] which are qualitatively very similar to those obtained in the ^{40}Ar bombardments. For Tb the charge distributions[30] are

still broad (although narrower than those for Ag); however, the angular distributions show weak side peaking near the projectile. The Ta charge distributions[31] are narrower than those of Tb, but somewhat broader than in the Au case. The side peaking in the angular distributions is well developed for Ta, but does not persist for as many elements as in the Au case.

The continuous evolution in the behavior of the angular distribution appears to be correlated[22] with the ratio E/B. For the systems 620 MeV Kr + Ag, Tb, Ta and Au, the ratio E/B is 1.9, 1.7, 1.6 and 1.5, respectively. For E/B less than about 1.6, strong side peaking is observed in the angular distributions. When this ratio is much greater than 1.6, forward peaking is observed. Recent experimental results[32,33] for Ag + 170 MeV and 200 MeV ^{40}Ar (E/B = 1.2 and 1.4, respectively) also show strong focusing effects in the angular distributions. This point is discussed in more detail in refs. 22 and 23 .

3.5 DEPENDENCE OF THE CHARGE AND ANGULAR DISTRIBUTIONS ON ENERGY DISSIPATION

The energy spectra observed in "light ion" reactions and in the reaction Ag + 620 MeV Kr were bimodal near the grazing angle and a decomposition of the relaxed and quasi-elastic was justifiable. In the current reaction the quasi-elastic and relaxed components are not resolvable. In fact only very broad energy distributions are observed at angles near the grazing angle, and thus it is of considerable importance to determine the energy dependence of the charge and angular distributions.

To this end, we have adopted a procedure for producing charge and angular distributions for various energy windows, or "bins", relative to the relaxed energy line. The energy windows are defined by a series of $E_{fragment}$ vs. Z lines parallel to the experimental mean relaxed energies as determined from measurements at forward and backward angles, where the energy spectra are essentially relaxed (see Fig. 2).

The dependence of the integrated (over angle) charge distributions on the degree of energy dissipation is illustrated in Fig. 11. The degree of energy dissipation increases with decreasing window number (i.e. from top to bottom of Fig. 11). The qualitative interpretation of this figure is clear. In the early stage of energy dissipation (large energies or large bin numbers, the Z-distributions are narrow or "young". For larger degrees of damping, the charge distributions become progressively broader or "older". The position of the centroids is strongly correlated with the Z-distribution widths. The narrow distributions show essentially no shift from the projectile atomic number. However, as the distributions broaden, the centroid moves to somewhat larger atomic numbers, in accordance with potential energy considerations (secondary fission of Au-like fragments may also contribute to the shift in centroid for the low energy bins). The overall behavior of the Z-distributions shows that the diffusion along the mass asymmetry mode is coupled to the energy relaxation. The variation of the Z-distribution widths with energy damping has been discussed by Huizenga et al.[34]

The angular distributions of several energy windows (see Fig. 12) show a very interesting feature (note that $d\sigma/d\theta$ is plotted and that a

1/sin θ distribution for $d\sigma/d\Omega$ would be here a horizontal line). For small energy losses (shaded squares and open triangles) the side peaking is very strong. This is not unexpected if one associates these bins with quasi-elastic transfer (short complex lifetimes). For progressively larger energy losses (longer lifetimes), the peaking becomes less pronounced; and, for the lowest energy windows (circles), the distributions are forward peaked (straight line with negative slope). One should note that the side peak appears to be somewhat more persistent for atomic numbers closer to the projectile (the anomalous behavior for some elements at backward angles results from kinetic energies somewhat higher than the average in this region, and is discussed in the next section). From these angular distributions one may conclude that the lowest kinetic energy products are associated with longer decay times as manifested by forward rather than side peaking of their angular distributions.

3.6 WILCZYNSKI DIAGRAMS

In interpreting the data it is useful to produce contour diagrams like those first made by Wilczynski.[35] A few representative examples are given in Fig. 13. These plots have been generated by linearly interpolating between adjacent experimental center-of-mass spectra and were drawn with the aid of a CDC-7600 computer. The spectra have been converted to E_{total} vs θ_{cm} and contours have been drawn through points of constant $\partial^2\sigma/\partial\theta_{cm}\partial E_T$; thus, a $1/\sin\theta$ distribution appears on such a plot as a series of parallel horizontal contours.

The deep-inelastic component manifests itself as a ridge at low energies, approximately parallel to the θ-axis. For Z's well above or

well below the projectile, this ridge constitutes the only major structure. For all elements, forward peaking in excess of $1/\sin\theta$ is observed (see Fig. 13). The behavior for high Z's (particularly Z = 44 and 46) at backward angles is not well understood. Secondary fission may be the cause of this distortion of the deep inelastic ridge. However, this increasing energy observed at back angles may be due to experimental errors, and/or errors in the relatively large energy corrections for high atomic numbers cannot be ruled out. Note also that the conversion to the total center-of-mass energy amplifies the absolute disagreement.

Atomic numbers closer to the projectile exhibit a second concentration of cross section at small center-of-mass angles, generally associated with bulging towards higher energies reflecting the coupling of energy dissipation and mass diffusion. For Z's still closer to the projectile, Z = 34, 38 for example, a well defined quasi-elastic ridge develops. This ridge attains its maximum energy slightly inside the grazing angle (60° from Table I), and moves rapidly towards lower energies for smaller angles. The slope of the quasi-elastic ridge is considerably steeper here than in the case[29] of Ag + 620 MeV Kr or in light ion bombardments high above the interaction barrier. This sharp descent of the quasi-elastic ridge is the reason that near the grazing angle only a single very broad peak is visible in the kinetic energy spectra. This claim is supported by the case of Ag + 620 MeV Kr where the gentler slope results in bimodal kinetic energy spectra.[29]

4. Conclusion

The dominant influence of the interaction time on the character of the charge and angular distributions produced in heavy ion reactions is clearly visible in the ^{197}Au + 620 MeV ^{86}Kr data. The evolution from side to forward peaked angular distributions with both increasing energy dissipation and increasing mass transfer beautifully illustrates the transition from short to long lifetimes for the intermediate complex. This transition is also seen in the evolution of the charge distributions from narrow ("young") to broad ("old") with energy dissipation and with lab angle. The differences between the deep-inelastic and quasi-fission behavior appear to be related to differences in the lifetime of the reaction intermediate.

The complicated patterns observed in the charge and angular distributions are quantitatively reproduced by a diffusion model calculations incorporating an ℓ-dependent lifetime of the intermediate complex and an interpenetration of the two fragments. In particular, the peak magnitude, position and width of the integrated charge distribution as well as the angular dependence of the charge distribution are reproduced. Furthermore, the calculated position of the side peaking in the angular distributions and its evolution with mass transfer are in good agreement with the data. This overlap between theory and experiment for the ^{197}Au + 620 MeV ^{86}Kr and the previous agreement found for the ^{107,109}Ag + 288 MeV Ar system demonstrates that the diffusion model holds over a large mass range of projectile and target combinations, thus providing a unified picture for the interpretation of heavy ion reaction phenomena.

Acknowledgments

The authors would like to express their thanks to J. Hunter, J. Moulton and M. Newman for their help in taking the data and to H. Grunder and the SuperHILAC crew for providing us with a good Kr beam.

References

1) J. Galin, D. Guerreau, M. Lefort, J. Peter and X. Tarrago, and R. Basile, Nucl. Phys. A159 (1970) 461.

2) A. G. Artukh, G. F. Gridnev, V. L. Mikheev, V. V. Volkov and J. Wilczynski, Nucl. Phys., A215 (1973) 91.

3) L. G. Moretto, D. Heunemann, R. C. Jared, R. C. Gatti and S. G. Thompson, Physics and Chemistry of Fission 1973 (Intern. Atomic Energy Agency, Vienna, 1974), Vol. II, p. 351.

4) L. G. Moretto, S. K. Kataria, R. C. Jared, R. Schmitt and S. G. Thompson, Nucl. Phys., A255 (1975) 491.

5) R. Babinet, L. G. Moretto, J. Galin, R. Jared, J. Moulton and S. G. Thompson, Nucl. Phys., A258 (1976) 172.

6) J. Galin, L. G. Moretto, R. Babinet, R. Schmitt, R. Jared and S. G. Thompson, Nucl. Phys., A255 (1975) 472.

7) L. G. Moretto, J. Galin, R. Babinet, Z. Fraenkel, R. Schmitt, R. Jared and S. G. Thompson, Nucl. Phys., A259 (1976) 173.

8) L. G. Moretto, R. P. Babinet, J. Galin and S. G. Thompson, Phys. Lett., 58B (1975) 31.

9) B. Gatty, D. Guerreau, M. Lefort, J. Pouthas, X. Tarrago, J. Galin, B. Cauvin, J. Girard and H. Nifenecker, J. de Phys., 35 (1974) L117.

10) L. G. Moretto and J. S. Sventek, Phys. Lett., 58B (1975) 26.

11) F. Hanappe, M. Lefort, C. Ngô, J. Péter and B. Tamain, Phys. Rev. Lett., 32 (1974) 738.

12) K. L. Wolf, J. P. Unik, J. R. Huizenga, J. Birkelund, H. Freiesleben and V. E. Viola, Phys. Rev. Lett., 33 (1974) 1105.

13) L. G. Moretto, B. Cauvin, P. Glässel, R. Jared, P. Russo, J. Sventek and G. Wozniak, Phys. Rev. Lett., 36 (1976) 1069.

14) M. M. Fowler and R. C. Jared, Nucl. Instrum. and Methods 124, (1975) 341.

15) P. Glässel, R. C. Jared and L. G. Moretto, submitted to Nucl. Instrum. and Methods, Lawrence Berkeley Lab Report No. LBL-5084 (1976).

16) L. C. Northcliffe and R. F. Schilling, Nuclear Data Table A7 (1970) 233.

17) S. B. Kaufman, E. P. Steinberg, B. D. Wilkins, J. Unik, A. J. Gorski and M. J. Fluss, Nucl. Instrum. and Method, 115 (1974) 47.

18) B. Gatty, D. Guerreau, M. Lefort, J. Pouthas, X. Tarrago, J. Galin, B. Cauvin, J. Girard and H. Nifenecker, Z. Physik A273 (1975) 65.

19) B. Cauvin, R. C. Jared, P. Russo, R. Babinet and L. G. Moretto, to be published, LBL-5099.

20) P. Russo, B. Cauvin, P. Glässel, R. C. Jared, R. P. Schmitt, G. J. Wozniak and L. G. Moretto, submitted to Phys. Lett., LBL-5050.

21) W. Nörenberg, Phys. Lett., 53B (1974) 289.

22) L. G. Moretto and R. Schmitt, European Conference on Nuclear Physics with Heavy Ions, Caen, France (1976). LBL-5057.

23) L. G. Moretto and J. S. Sventek, Proceedings of the Symposium on Macroscopic Features of Heavy Ion Collisions, Vol. I, (1976), p. 235, Argonne National Lab Report No. ANL/PHY-76-2.

24) J. S. Sventek and L. G. Moretto, LBL-5012, submitted to Phys. Lett.

25) C. F. Tsang, Physica Scripta, 10A (1974) 90.

26) J. Randrup, private communication.

27) W. D. Myers, Nucl. Phys. A204 465 (1973).

28) J. R. Birkelund, J. R. Huizenga, H. Freiesleben, K. L. Wolf, J. P. Unik and V. E. Viola, Jr., Phys. Rev. C13 133 (1976).

29) R. P. Schmitt, P. Russo, R. Babinet, R. Jared and L. G. Moretto, to be published in Nucl. Phys. LBL-5042.

30) G. J. Wozniak, R. P. Schmitt, B. Cauvin, P. Glässel, P. Russo, and L. G. Moretto, to be published.

31) B. Cauvin, R. P. Schmitt, G. J. Wozniak, P. Russo, P. Glässel, and L. G. Moretto, to be published.

32) G. J. Wozniak, G. J. Mathews, G. Bizard, R. P. Schmitt, and L. G. Moretto, to be published.

33) G. J. Mathews, G. J. Wozniak, R. P. Schmitt, and L. G. Moretto, to be published.

34) J. R. Huizenga, J. R. Birkelund, W. U. Schröder, K. L. Wolf and V. E. Viola, Jr., Phys. Rev. Letters, 37 (1976) 885.

35) J. Wilczynski, Phys. Letters, 47B 484 (1973).

Table 1. Characteristics of the reaction $^{197}Au + ^{86}Kr$ at 620 MeV bombarding energy.

$E_{c.m.}$ (MeV)	432.
B(MeV)	282.
E/B	1.53
σ_R(b)	2.3
$\theta^{crit}_{c.m.}$ (deg)	58.
ℓ_{max} ($\hbar$)	302.
τ_{rot} (sec)	$9. \times 10^{-21}$

An r_o of 1.225 fm was used in calculating the nuclear radii. In addition, 2.0 fm were added to the sum of the radii in the calculations. The rotational period τ_{rot} is given for the entrance channel mass asymmetry and assumes $\ell = \ell_{r.m.s.}$ and spherical fragments.

Figure Captions

1) Center of mass kinetic energy spectra for representative elements (Z indicated only once on far left) detected in the reaction $^{197}Au + 620.MeV\ ^{86}Kr$ at three angles. See discussion in text. For reference the calculated Coulomb energy for two touching spheres($R = 1.225\ (A_1^{1/3} + A_2^{1/3}) + 2.0$ fm) of the indicated asymmetry is shown by a vertical arrow for each spectra.

2) Mean center-of-mass kinetic energies and widths; average of all angles where there was no evidence of a quasi-elastic component (open symbols), and an angle close to the grazing angle (40.4° — shaded symbols). The "error bars" shown correspond to one standard deviation from the mean and one should note that the very small standard deviations for large Z's (>50) are the result of few data points. The solid curve is the calculated energy expected from the Coulomb repulsion of two spherical fragments. The FWHM was calculated from 2nd moments of energy spectra assuming a gaussian shape. The small FWHM for Z = 36, relative to neighboring elements, is caused by the very intense quasi-elastic component.

3) Charge distributions for reaction products detected at several laboratory angles. The dashed lines indicate uncertainty in obtaining accurate cross sections for Z's close to the projectile due to large background contributions.

4) Ridge line potentials for the reaction ^{197}Au + 620 MeV ^{86}Kr. Each curve is labeled according to ℓ-wave.

5) Contours of constant population in the plane defined by the charge asymmetry coordinate and the time for four ℓ-waves and for the reaction ^{197}Au + 620 MeV ^{86}Kr. The sharpening of the population distributions at high ℓ-values is readily visible.

6) Calculated dependence of σ_z^2 vs $\bar{Z} - Z_o$ (Z_o = 36) for various ℓ-waves in the reaction ^{197}Au + ^{86}Kr at 620 MeV bombarding energy. The σ_z^2 vs $\bar{Z} - Z_o$ curve for the distribution obtained by integrating over ℓ with the $2\ell + 1$ weight is also shown.

7) Total experimental (circles) and calculated (heavy curve) cross sections, as a function of Z for the reaction ^{197}Au + 620 MeV ^{86}Kr. The data points were integrated from θ_{lab} = 10 - 80° and the thin line connecting the data points is to guide the eye.

8) Comparison between "experimental" and calculated Z distributions at various center-of-mass angles for the reaction ^{197}Au + 620 MeV ^{86}Kr. The "experimental" curve was obtained by linear interpolation between data points.

9) Center-of-mass angular distributions as a function of fragment atomic number for the reaction ^{197}Au + ^{86}Kr at 620 MeV bombarding energy. The curves drawn through the data points are to guide the eye.

10) Calculated (curves) and "experimental" (circles) angular distributions for the reaction ^{197}Au + 620 MeV ^{86}Kr.

11) Integrated (over angle) charge distributions for several kinetic energy windows for the reaction ^{197}Au + 620 MeV ^{86}Kr. The bin number multiplied by 20 gives the upper energy limit of the window in MeV for Z = 36. Window number 9 is approximately centered on the relaxed peak for all fragments (see discussion in text).

12) Center-of-mass angular distributions, $(d\sigma/d\theta)_{c.m.}$, for several kinetic energy windows and four selected elements.

13) Contours of constant $(d\sigma/d\theta)_{c.m.}$ in the plane defined by the fragment total kinetic energy (center-of-mass) and by the center-of-mass angle (Wilczynski plot) for a selected number of fragments from the reaction ^{197}Au + 620 MeV ^{86}Kr. The spacing of the contours is given by 2^3, 2^4,... μb/rad - MeV.

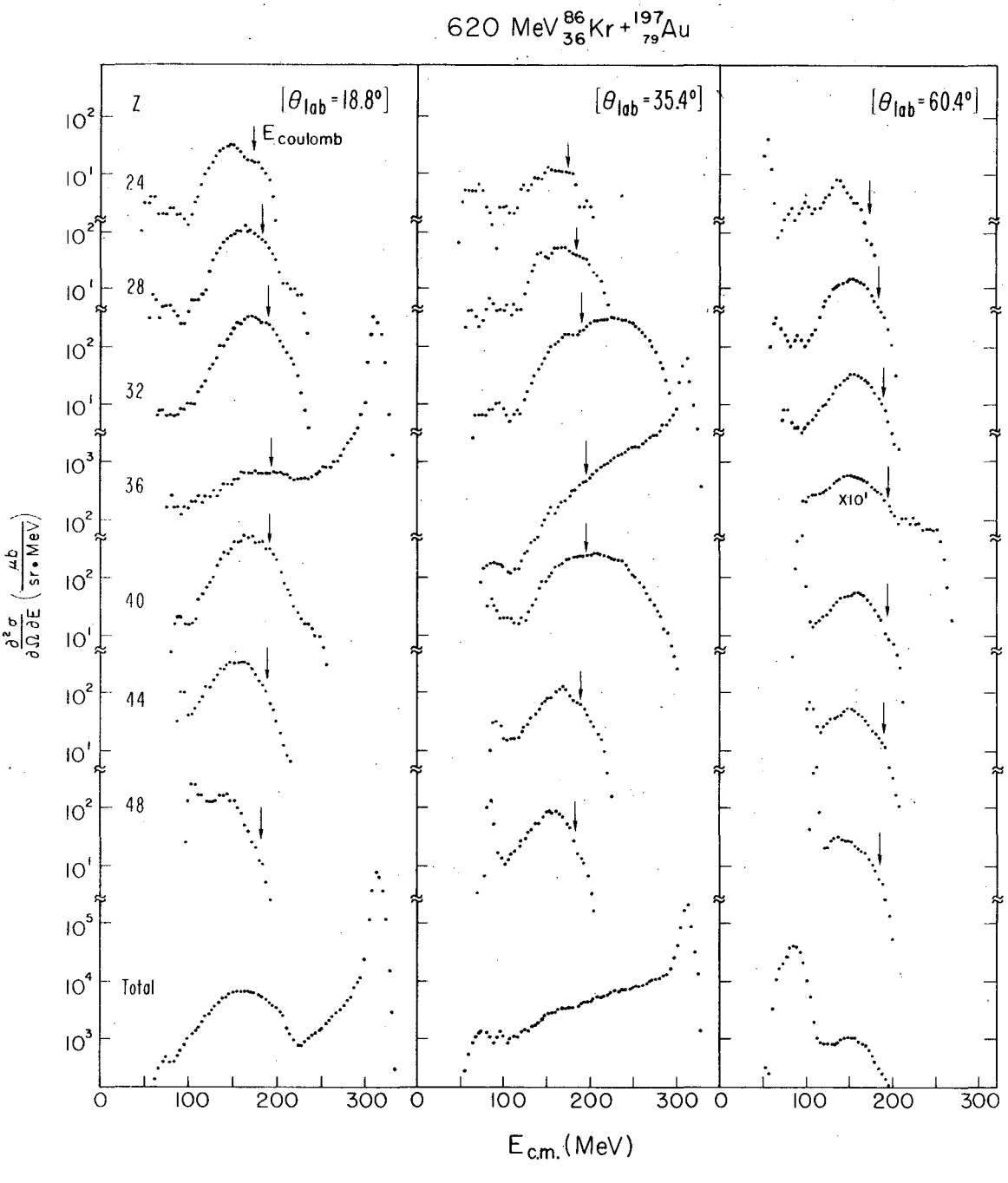
620 MeV $^{86}_{36}Kr + ^{197}_{79}Au$
Z
$[\theta_{lab} = 18.8°]$
$[\theta_{lab} = 35.4°]$
$[\theta_{lab} = 60.4°]$
$E_{coulomb}$
24
28
32
36
40
44
48
Total
X10'
$\frac{d^2\sigma}{d\Omega\, dE}\left(\frac{\mu b}{sr \cdot MeV}\right)$
$E_{c.m.}$ (MeV)
XBL 7610-4211

Fig. 1

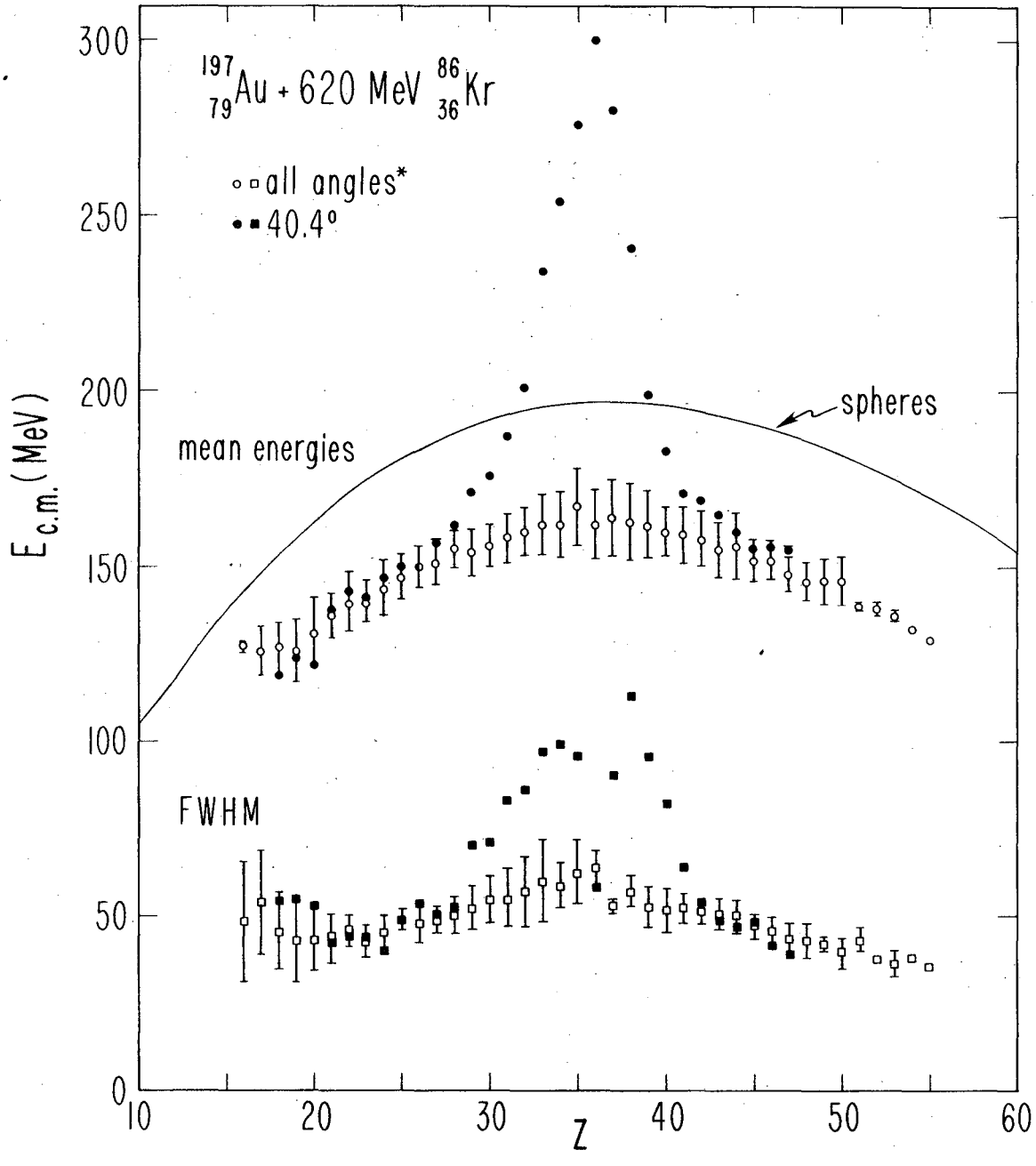

XBL 7611 4477

Fig. 2

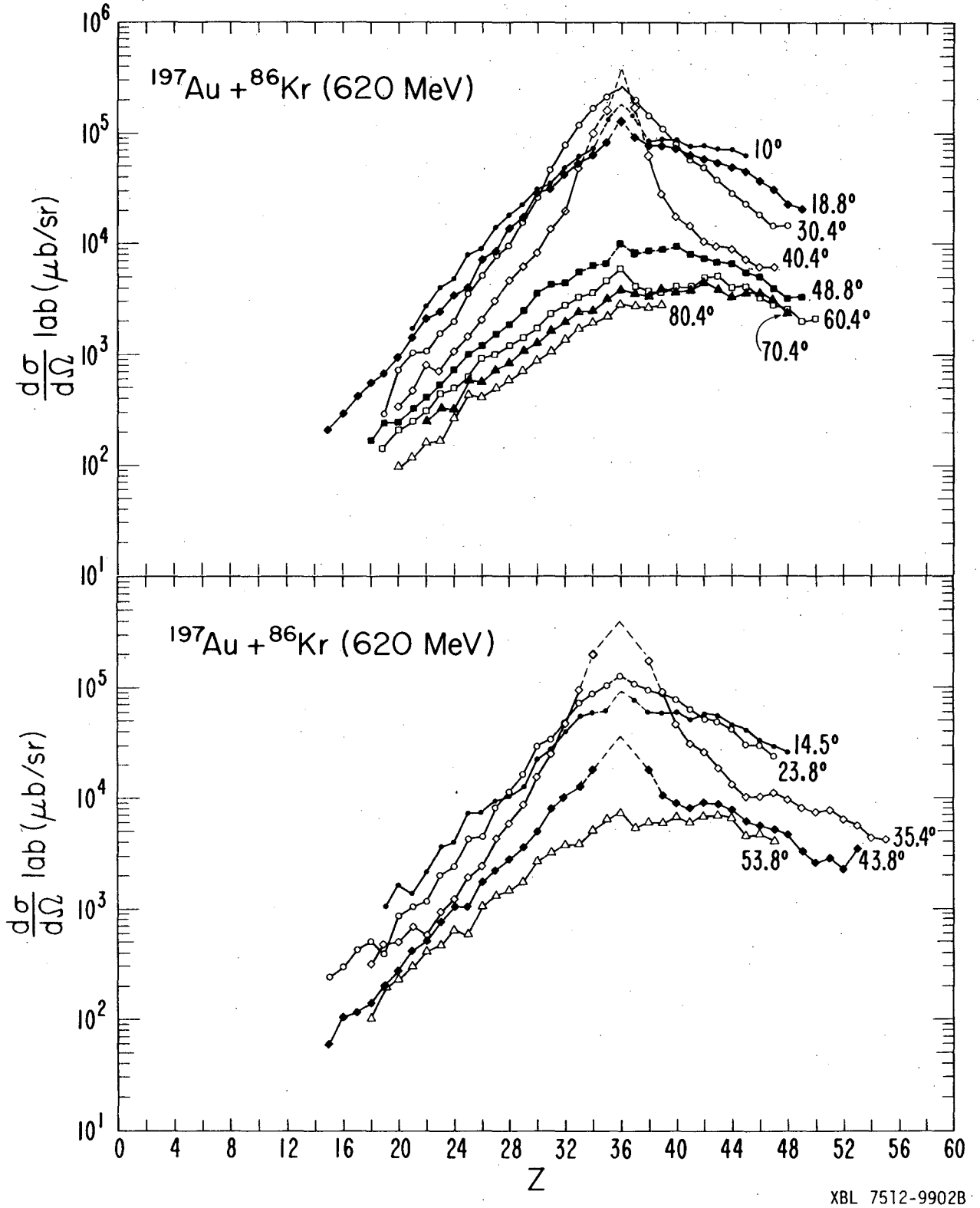
197Au + 86Kr (620 MeV)
10°
18.8°
30.4°
40.4°
48.8°
60.4°
70.4°
80.4°
dσ/dΩ lab (μb/sr)
197Au + 86Kr (620 MeV)
14.5°
23.8°
35.4°
43.8°
53.8°
Z
XBL 7512-9902B

Fig. 3

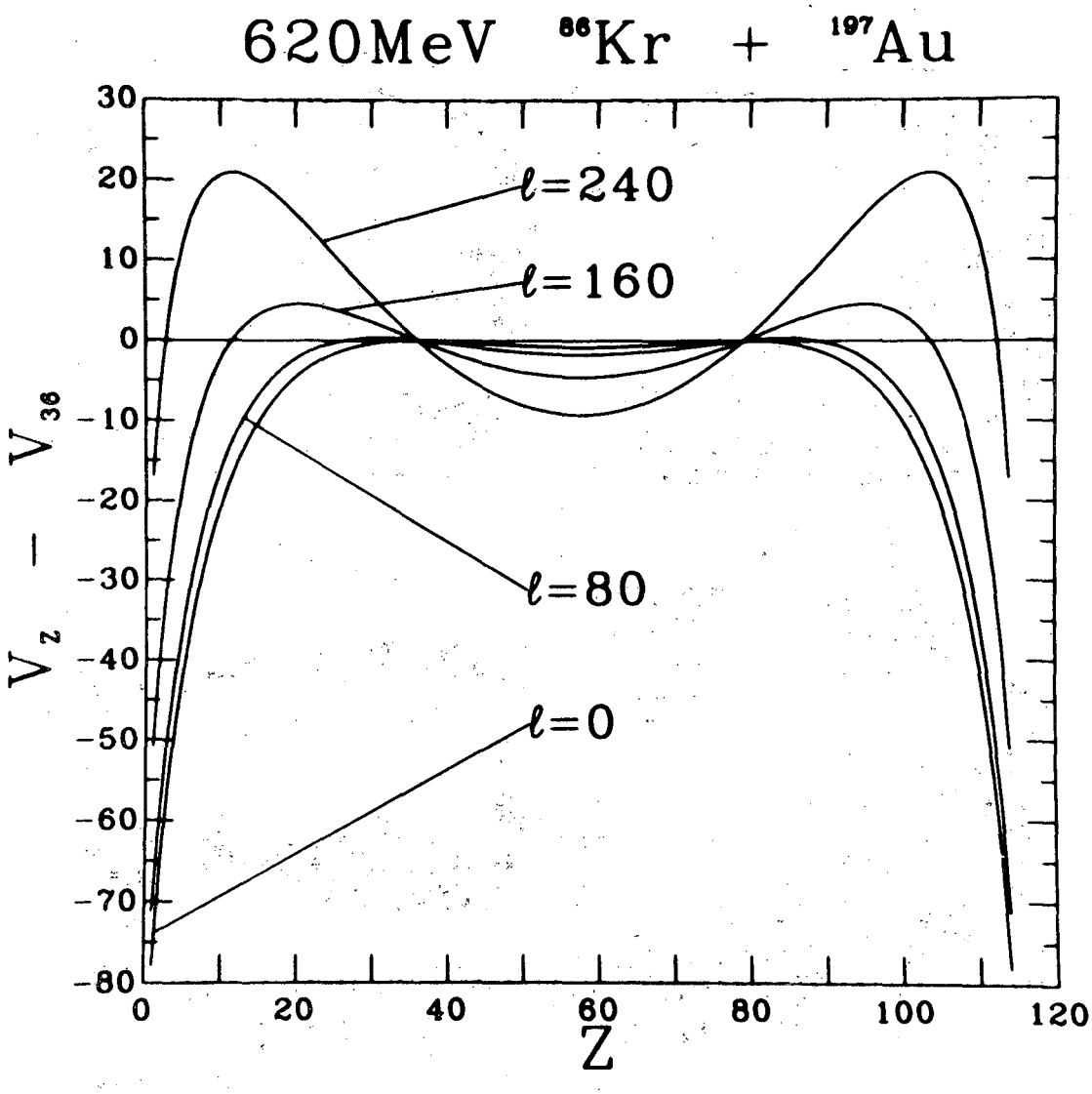

XBL 7611-9953

Fig. 4

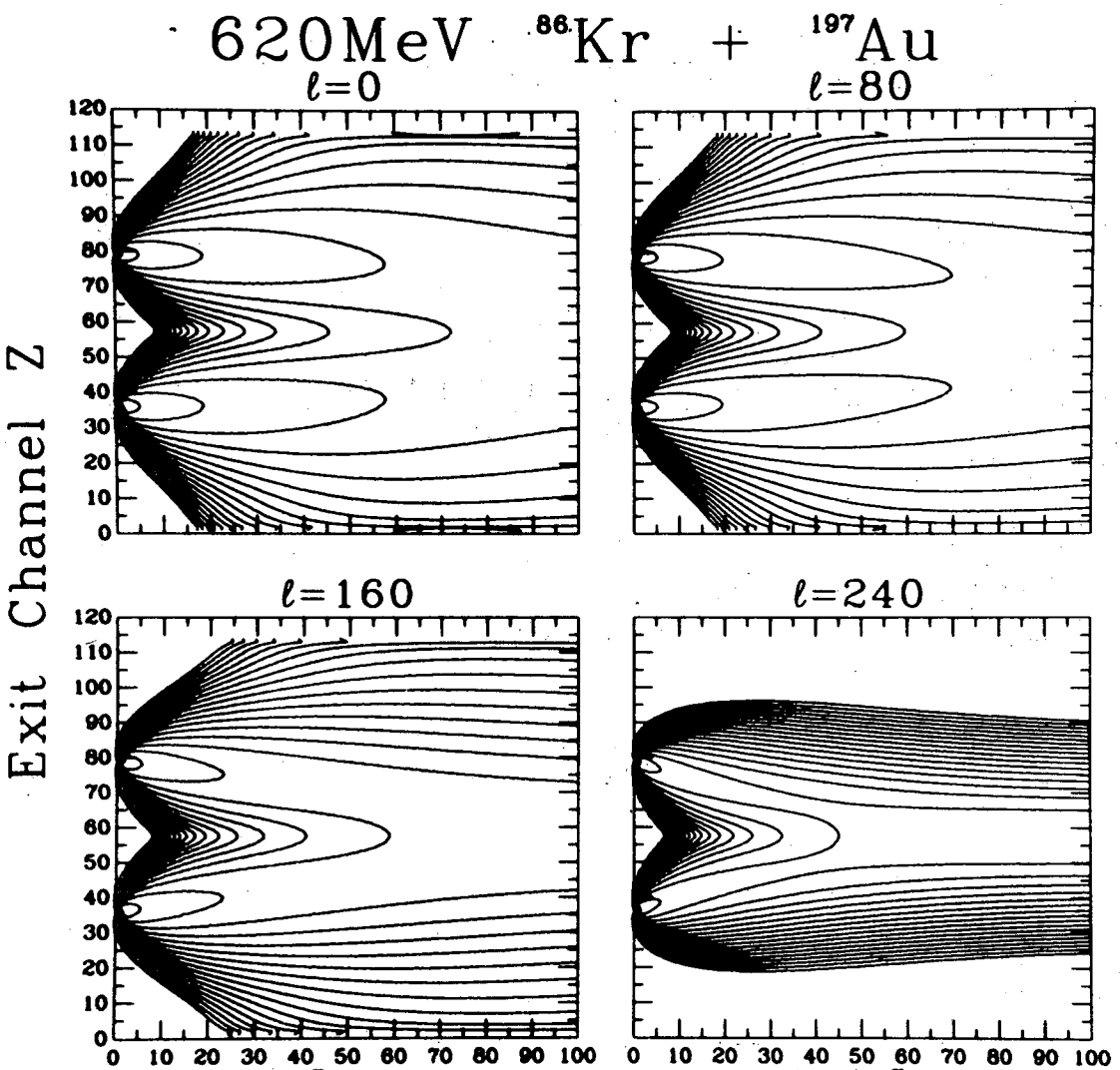
620MeV ^{86}Kr + ^{197}Au
ℓ=0
ℓ=80
ℓ=160
ℓ=240
Exit Channel Z
t [in units of 10^{-22}sec]
XBL 7611-9902

Fig. 5

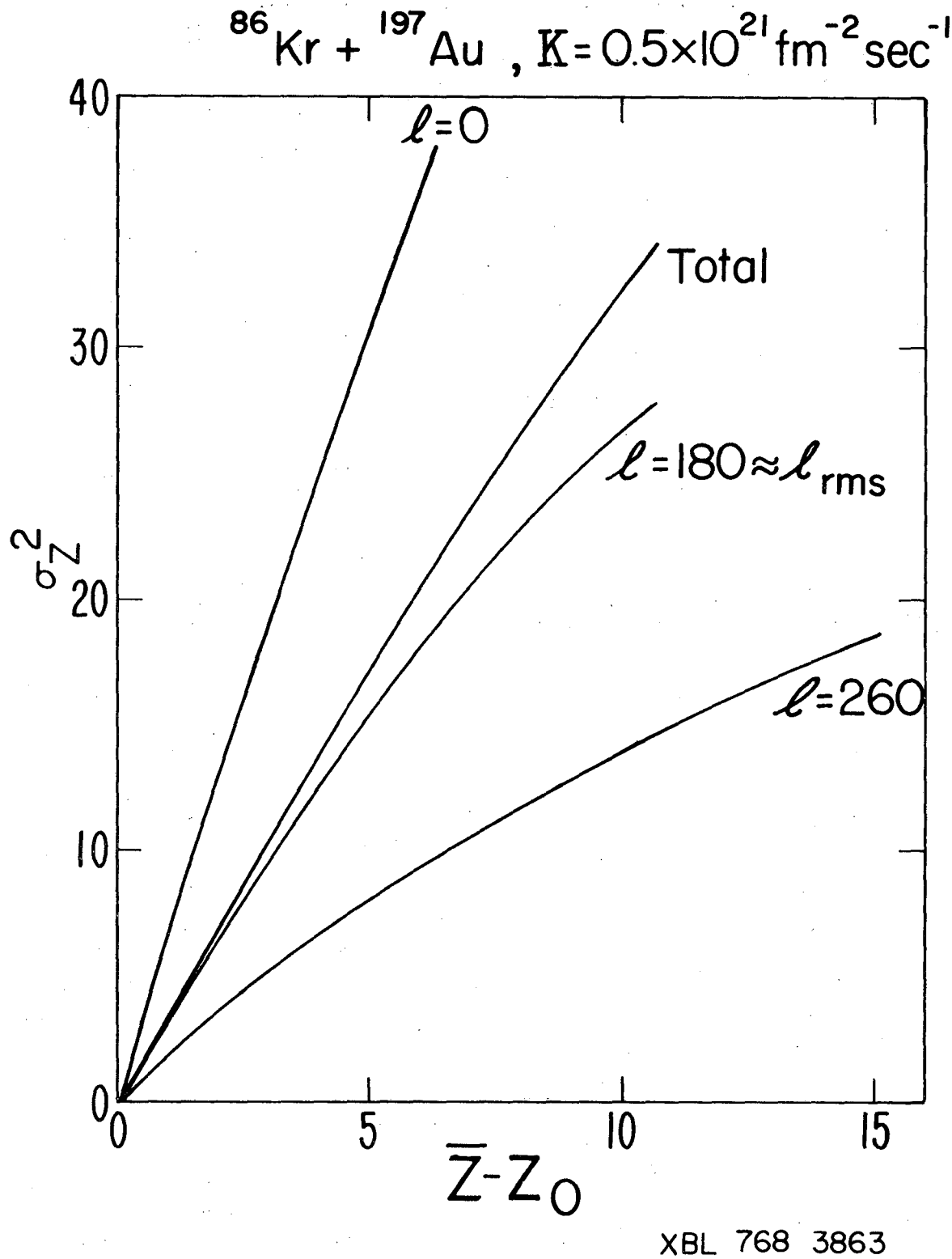

Fig. 6

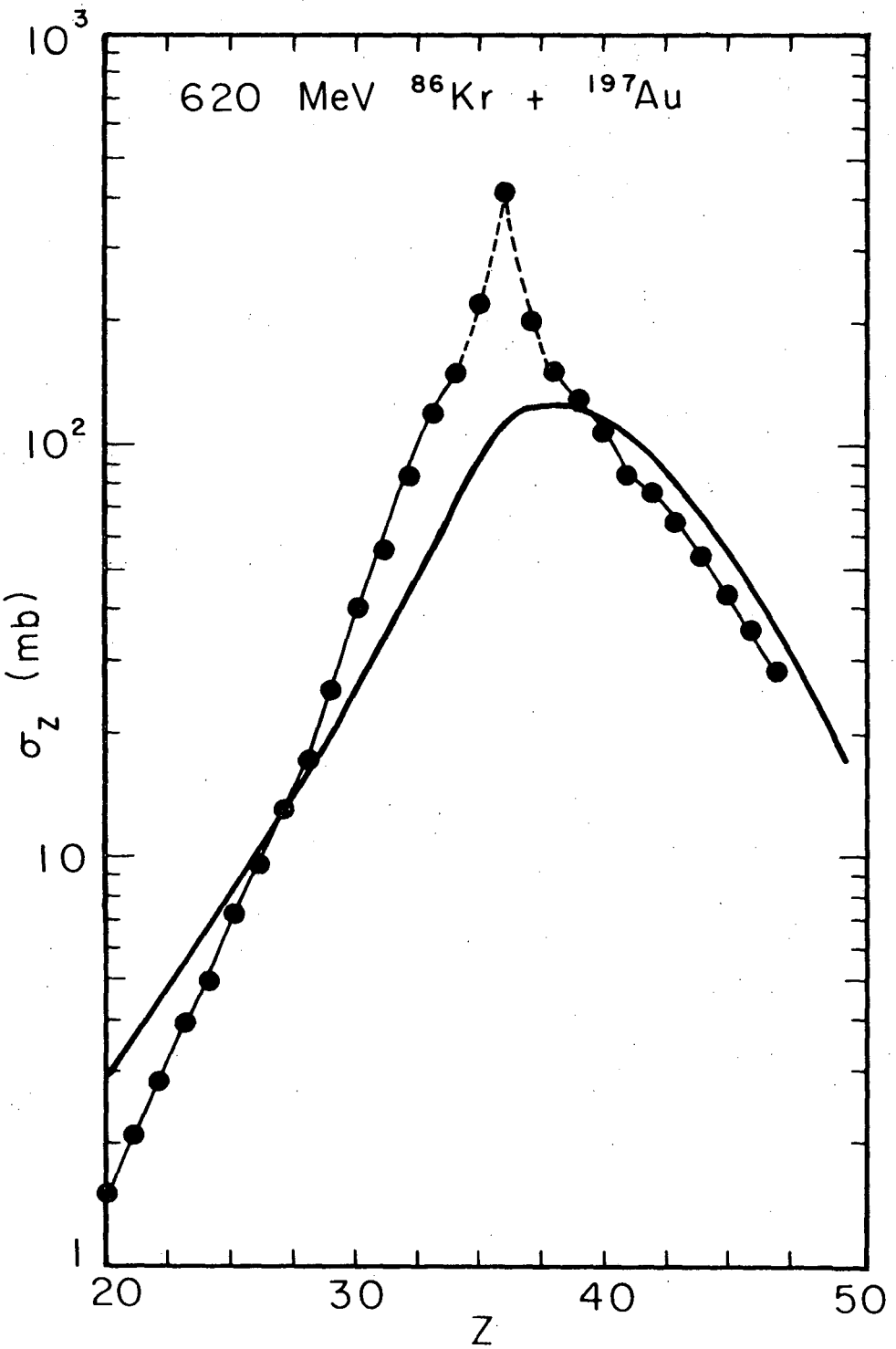

XBL7611-4461

Fig. 7

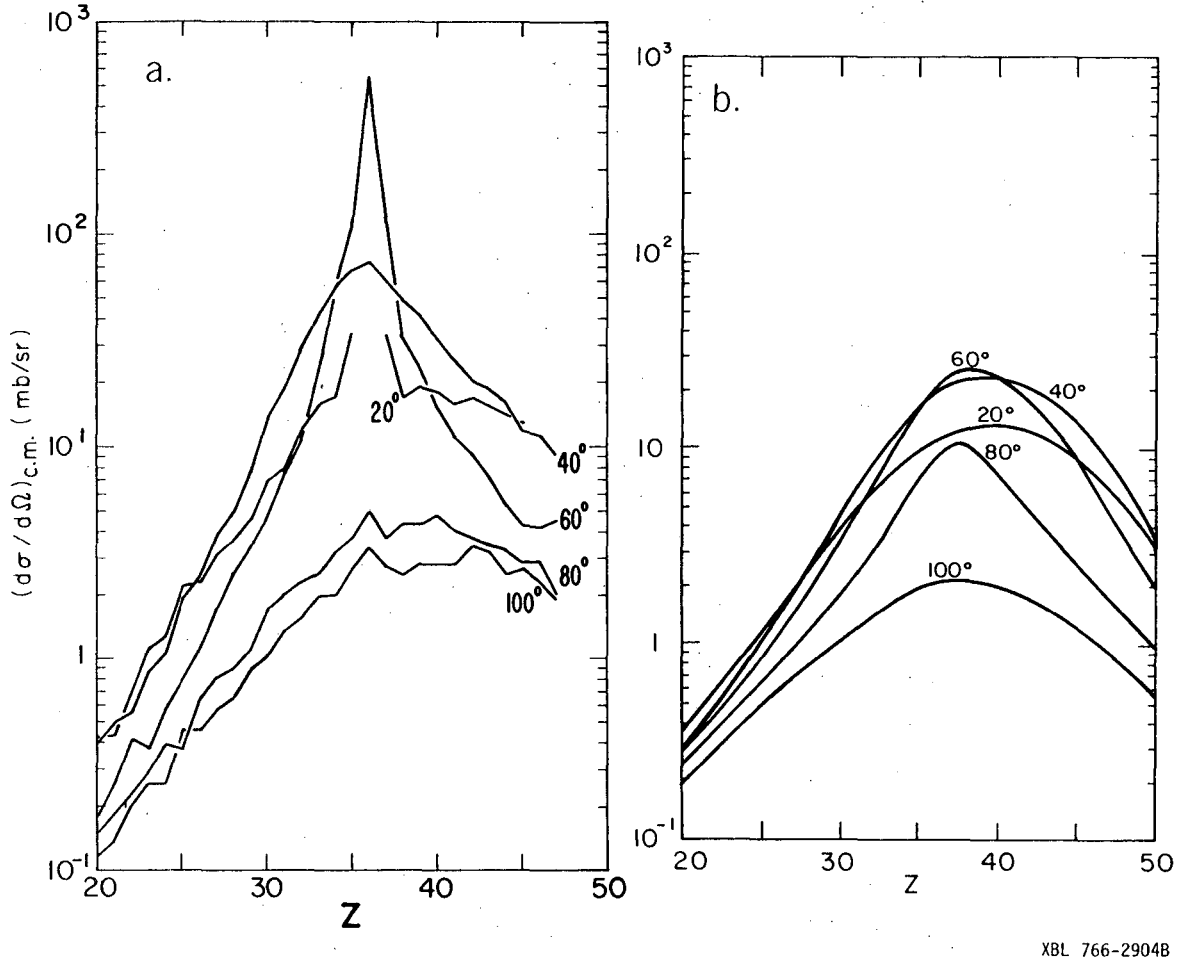

XBL 766-2904B

Fig. 8

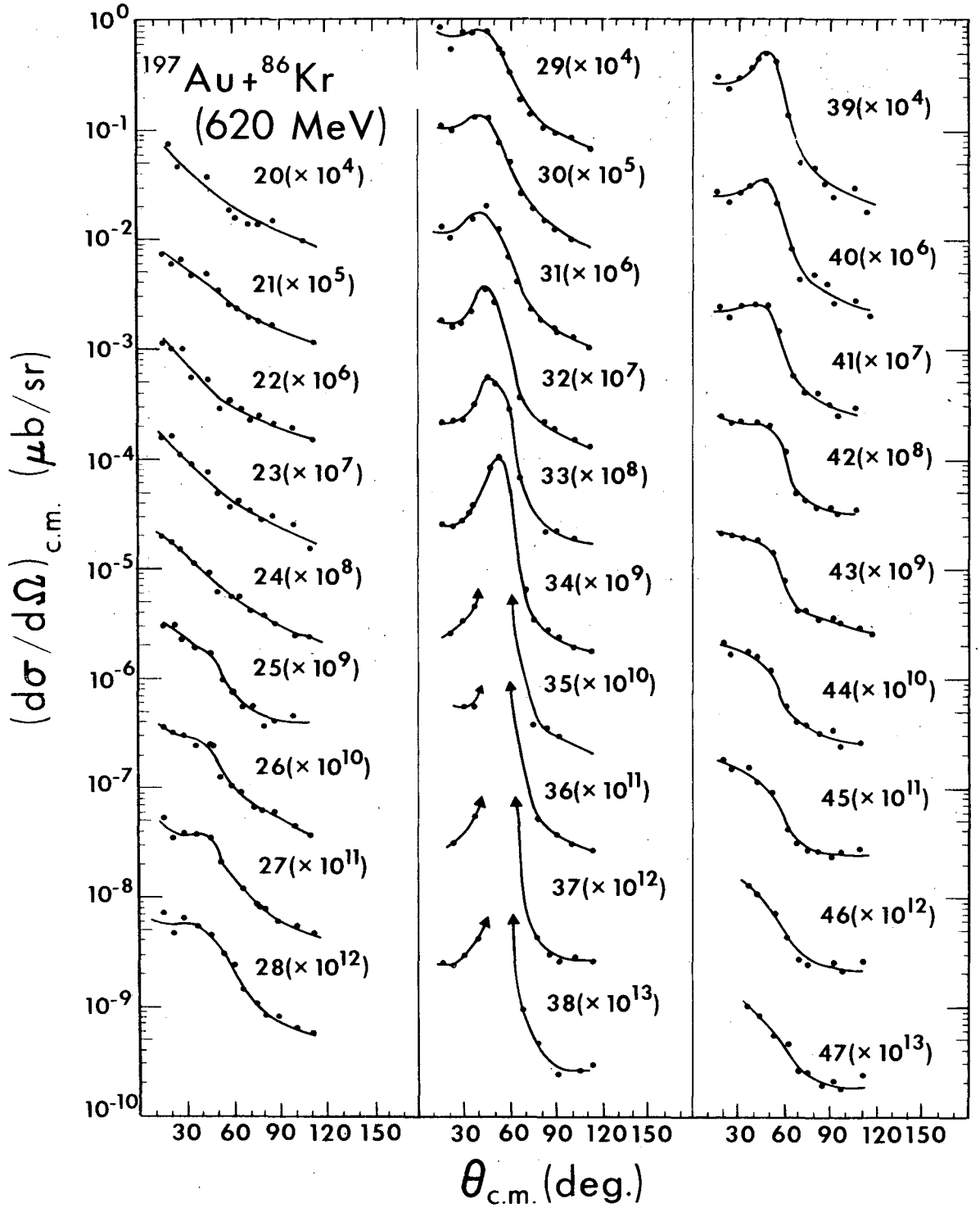

XBL 7512-9891

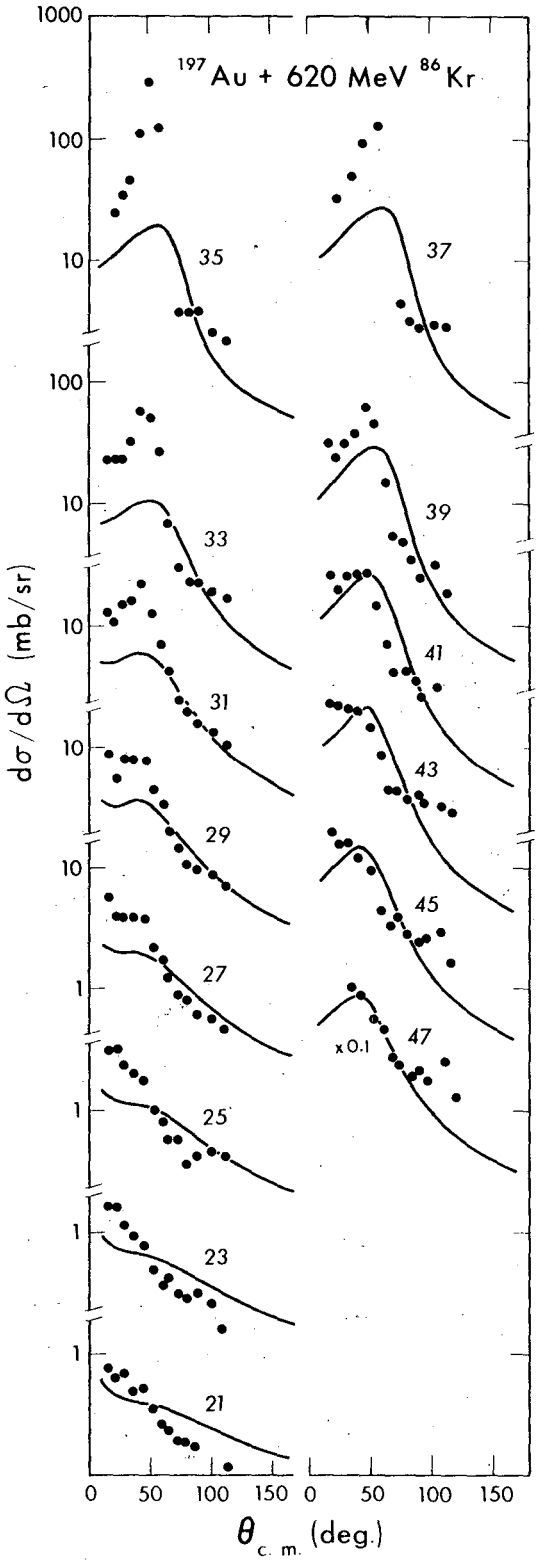

XBL 7611-4486

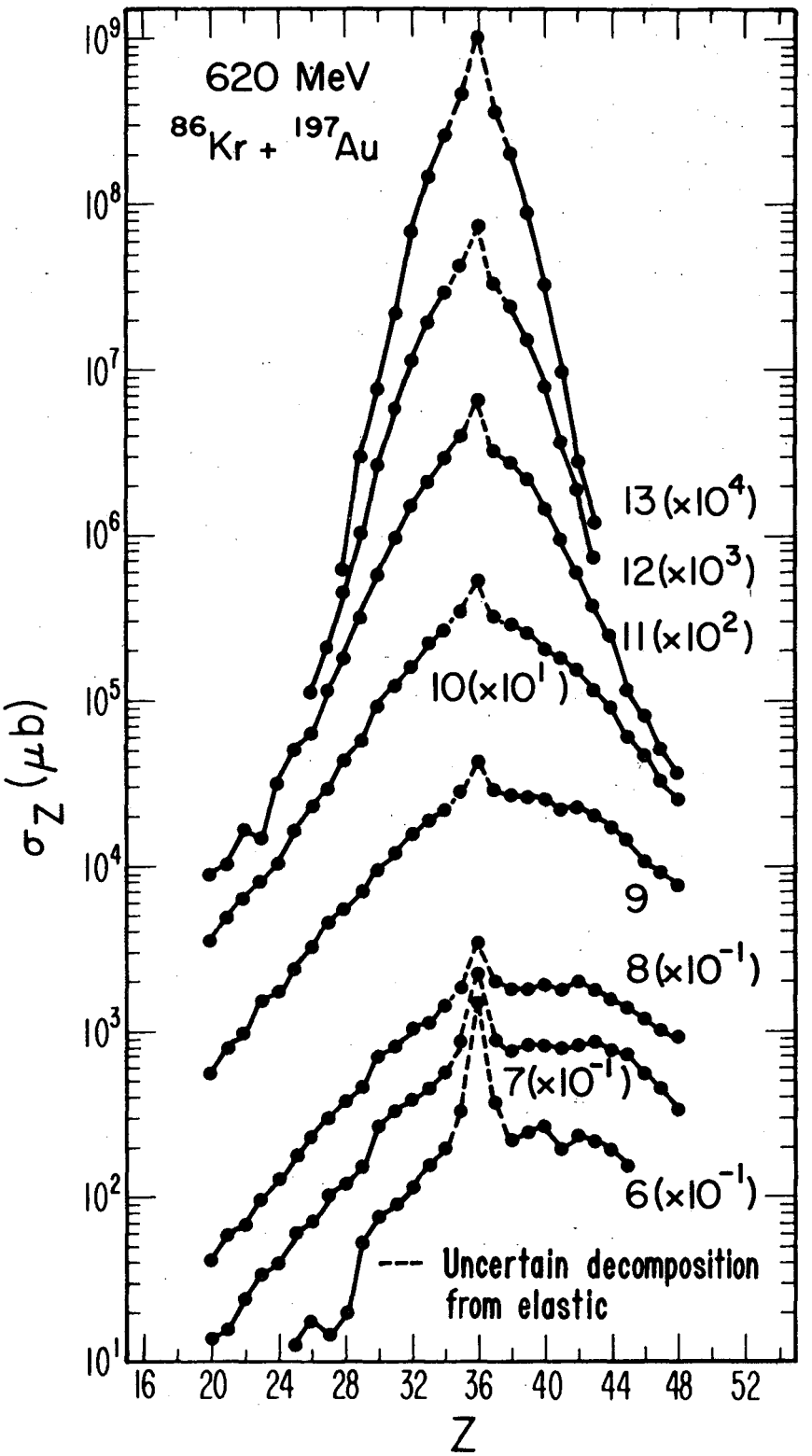

Fig. 11

XBL 768-10149

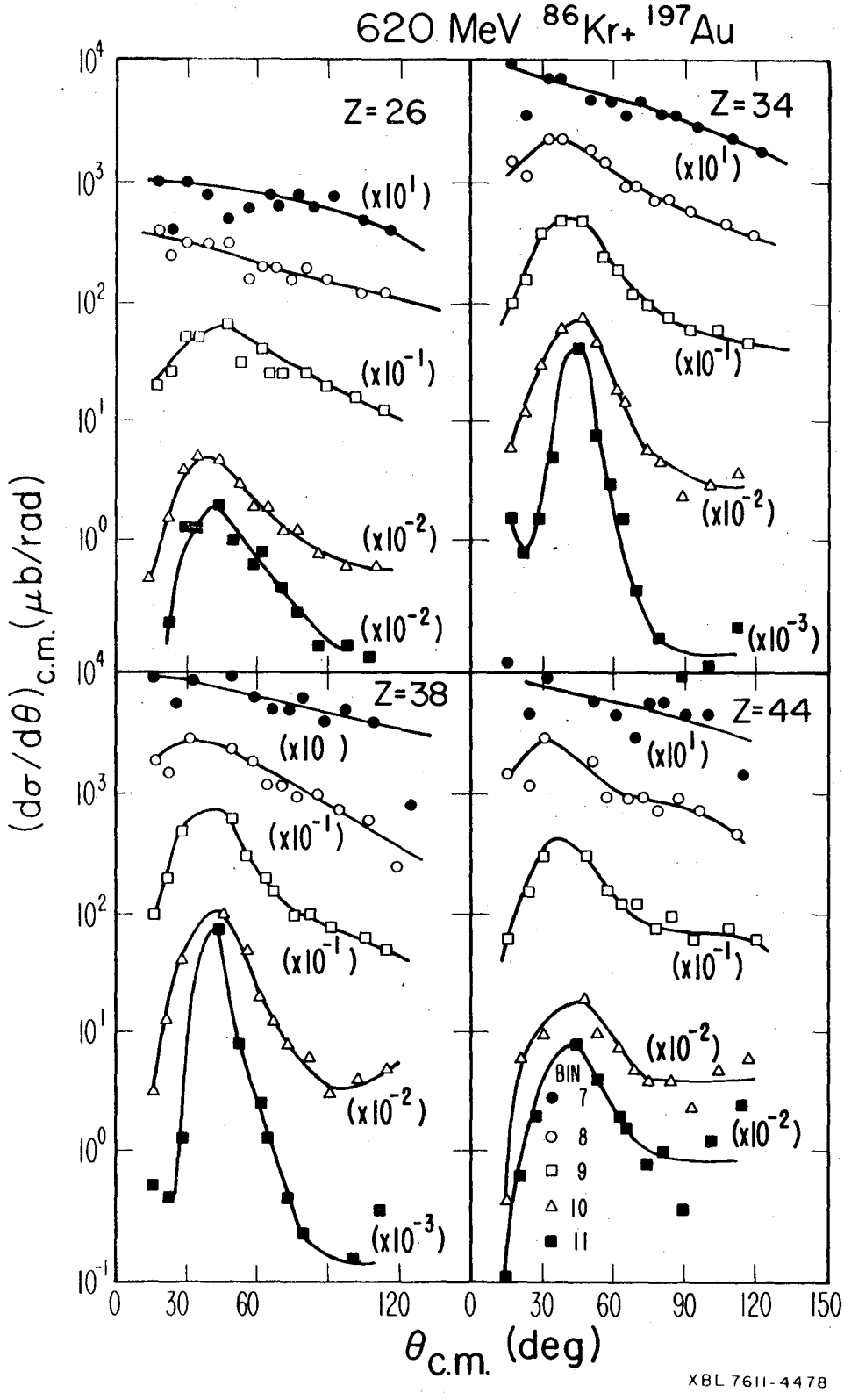

Fig. 12

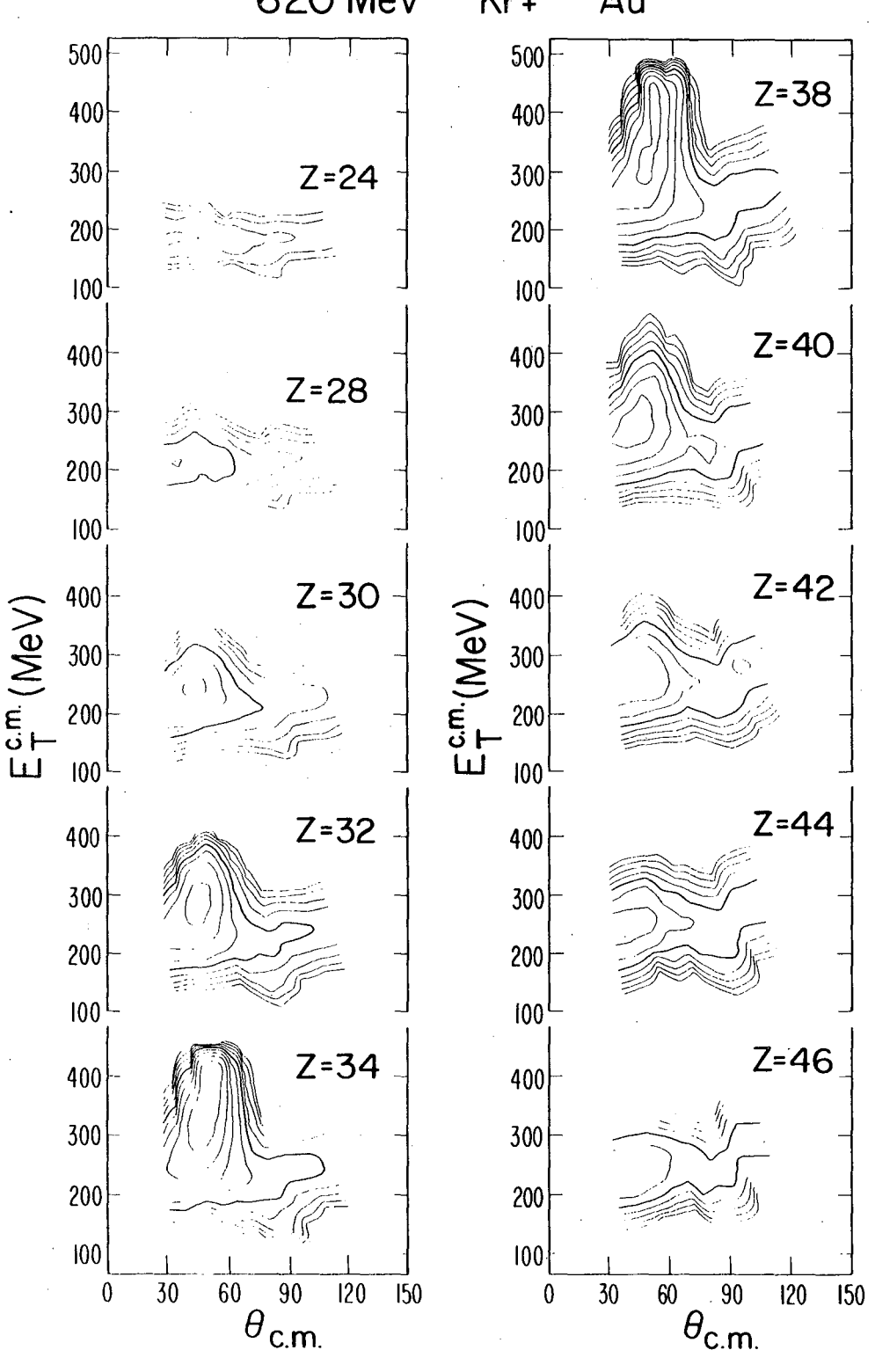
620 MeV 86Kr + 197Au
Z=24
Z=28
Z=30
Z=32
Z=34
Z=38
Z=40
Z=42
Z=44
Z=46
E_T^c.m. (MeV)
θ c.m.
0 30 60 90 120 150
100 200 300 400 500
XBL 769 4077

Fig. 13

TECHNICAL INFORMATION DIVISION
LAWRENCE BERKELEY LABORATORY
UNIVERSITY OF CALIFORNIA
BERKELEY, CALIFORNIA 94720